Study of Alpha Background in a Dark Matter Detector

by

Hayk Yegoryan

Submitted to the Department of Physics
in partial fulfillment of the requirements for the degree of

Bachelor of Science in Physics

at the

MASSACHUSETTS INSTITUTE OF TECHNOLOGY

June 2010

Author .....
Department of Physics
May 18, 2010

Certified by .....
Denis Dujmic
Research Scientist
Thesis Supervisor

Certified by .....
Gabriella Sciolla
Associate Professor of Physics
Thesis Supervisor

Accepted by .....
David E. Pritchard
Senior Thesis Coordinator, Department of Physics

Study of Alpha Background in a Dark Matter Detector

by

Hayk Yegoryan

Submitted to the Department of Physics
on May 8, 2010, in partial fulfillment of the
requirements for the degree of
Bachelor of Science in Physics

Abstract

Alpha background, specifically from radon and its progeny in the uranium and thorium chains, has been a major issue in dark matter detectors. This work focuses on alpha background presence in the DMTPC experiment by examining the energy distribution and the rate of alpha tracks in detector's fiducial volume. It was found that the rate and the energy distribution of alpha tracks are inconsistent with radon buildup in the detector. This was verified by replacing stainless steel materials with copper that is known to have lower uranium concentration. The alpha background was reduced 5 fold confirming that the origin of alphas is from early uranium decay chain, not radon buildup in the detector.

Thesis Supervisor: Denis Dujmic
Title: Research Scientist

Thesis Supervisor: Gabriella Sciolla
Title: Associate Professor of Physics

Acknowledgments

I would like to thank everybody on the DMTPC team for their support and their availability for help: Jeremy, Cosmin, Liam, James, Jocelyn, Ian, Sean, Asher, and all the others with whom I have come in contact, whether direct or indirect.

I'd like to extend a warm thank you to Prof. Peter Fisher, who has not only been supportive but also very instructive and inspirational throughout my three years with the program. A special thanks also goes to Prof. Gabriella Sciolla who introduced me to the DMTPC experiment at first and remained a very steady guide throughout the process. Her personal and particular attention toward my success both as a scientist and an individual is very greatly appreciated.

Finally, I'd like to extend a special dedication to Denis Dujmic. Without him this paper would never have come to completion. He has been nothing short of a father figure in my growth and maturation as a scientist. I am deeply grateful for all the hours of work he put into making sure that I understand every part of the experiment, and for his patience whenever I didn't.

Contents

List of Figures

List of Tables

Chapter 1

INTRODUCTION

1.1 Search for Dark Matter

There are a lot of cosmological phenomena that can not be explained using only the current scope of discovered matter in the universe. Orbital velocities of galaxies in clusters [1], as well as rotational velocities within the galaxies themselves [2], gravitational lensing [3, 4], the Bullet Cluster [5] and fluctuations in the CMB temperature [6] can all be explained using the current theories on Dark Matter. NASA's WMAP observations combined with measurements from Baryon Acoustic Oscillation in the distribution of galaxies, and Hubble constant within the Λ-CDM cosmological model conclude that non-baryonic dark matter comprises 83% of all the matter in the universe [6]. Although ample the evidence for existance of dark matter comes through its gravitational effect, nobody has yet been able to detect dark matter particles and measure other properties, such as mass, spin, interaction cross sections with regular matter.

There are currently many experiments [7] working toward the detection of Weakly Interacting Massive Particles (WIMPs) - the most popular candidates for Dark Matter. A very brief outline of these experiments is provided in Appendix C. Among them is a collaboration of MIT, Brandeis, and BU, called the Dark Matter Time Projection Chamber (DMTPC) which is to detect WIMPs with a sensitivity for their direction of movement.

There is a large halo of dark matter particles encompassing our galaxy. As the Earth spins around the Sun which spins around the galaxy, the Earth passes through this halo of particles. From our perspective, there is a wind of WIMPs coming from a very specific direction with a speed of $\sim$ 200 km/s (the rotational speed of the galaxy in the dark matter halo). Additionally, the direction will change by approximately (depending on latitude) 90° every 12 hours [8].

Dark matter detectors need to be large due to low interaction cross section of WIMPs with detector material. However, large detectors are very efficient in detecting natural background radiation that has several orders of magnitude higher rate than the WIMP interaction. Like the other experiments, the DMTPC requires reduction in environmental backgrounds for successful operation. This thesis is a study of alpha background that is one of the most important backgrounds in dark matter detectors.

1.2 Backgrounds in Dark Matter Searches

All dark matter experiments, DMTPC included, require extremely low backgrounds for operation. Most background comes from photons, electrons, neutrons, and alpha particles, with at least 6 orders of magnitude higher rate than the dark matter signal. Neutron background, as well as background caused by cosmic rays can be suppressed through passive shielding and positioning the detector underground. Other background can be reduced by discounting all events that do not have the corresponding energy, length of track, or the direction of WIMPs.

In general, any background that comes from outside of the detector can be dealt with relatively easily. Most external radiation can be shielded, or at the very least, discriminated from WIMPs. Problems start arising, however, when sources of background find themselves within the detector.

Most alphas comes from decay chains of uranium and thorium that are present in trace amounts in detector materials like stainless steel. Both of these have a double effect - they: (a) create alphas that interact with other nuclei from material to release neutrons that can cause a WIMP-like recoil, and (b) cause alpha and nuclear recoils

that can be directly seen in the detector.

1.2.1 Alpha Background

A comprehensive list of uranium chain progeny with their respective decay information is given in Table 1.1. The decay ranges and energies can also be seen plotted in Figure 1-2. Most of energy in the alpha decay is taken by a lighter alpha particle (4.2 - 7.7 MeV), while a heavier nucleus recoils carries less energy (72-146 keV).

In the uranium/thorium chains, radon is a particularly noteworthy culprit. It is gaseous, and so can break loose and travel into the sensitive region of the detector. Radon comes in two flavors – ^{220}Rn from the thorium decay chain, and ^{222}Rn from the uranium decay chain (There are more than two isotopes, but we are not concerned with those since their concentrations are negligible). Since uranium and thorium can both be found in trace amounts in most materials, it is very likely that some amount of radon will form inside the detector.

One of the most important attributes of radon that pertains to its contribution to background is its gaseous consistency. As such, radon that has been liberated from any decay chain can flow freely inside the detector. Although the alpha decay energy - 5.59 MeV for ^{222}Rn or 6.288 MeV for ^{220}Rn - falls far above our threshold, radon daughters in the decay chain are ionized and tend to stick to dust or components (e.g. the cathode plate) inside the active part of the detector (Figure 1-1).

Once stuck to the plate, the radon decay chain daughters that are prone to releasing alpha radiation will do so and recoil. If they happen to release the alpha out of the detector and recoil into the active volume of the detector, they will produce a track of similar length to recoils caused by WIMPs without an accompanying alpha track to veto. Additionally, most of the daughters are long-lived radioactive isotopes and will tend to be a source of background for a very long time.

The effects of the alpha background, as well as its origins in the DMTPC are not well enough understood. A purpose of this thesis is to characterize alpha background and look into possible ways of reducing it.

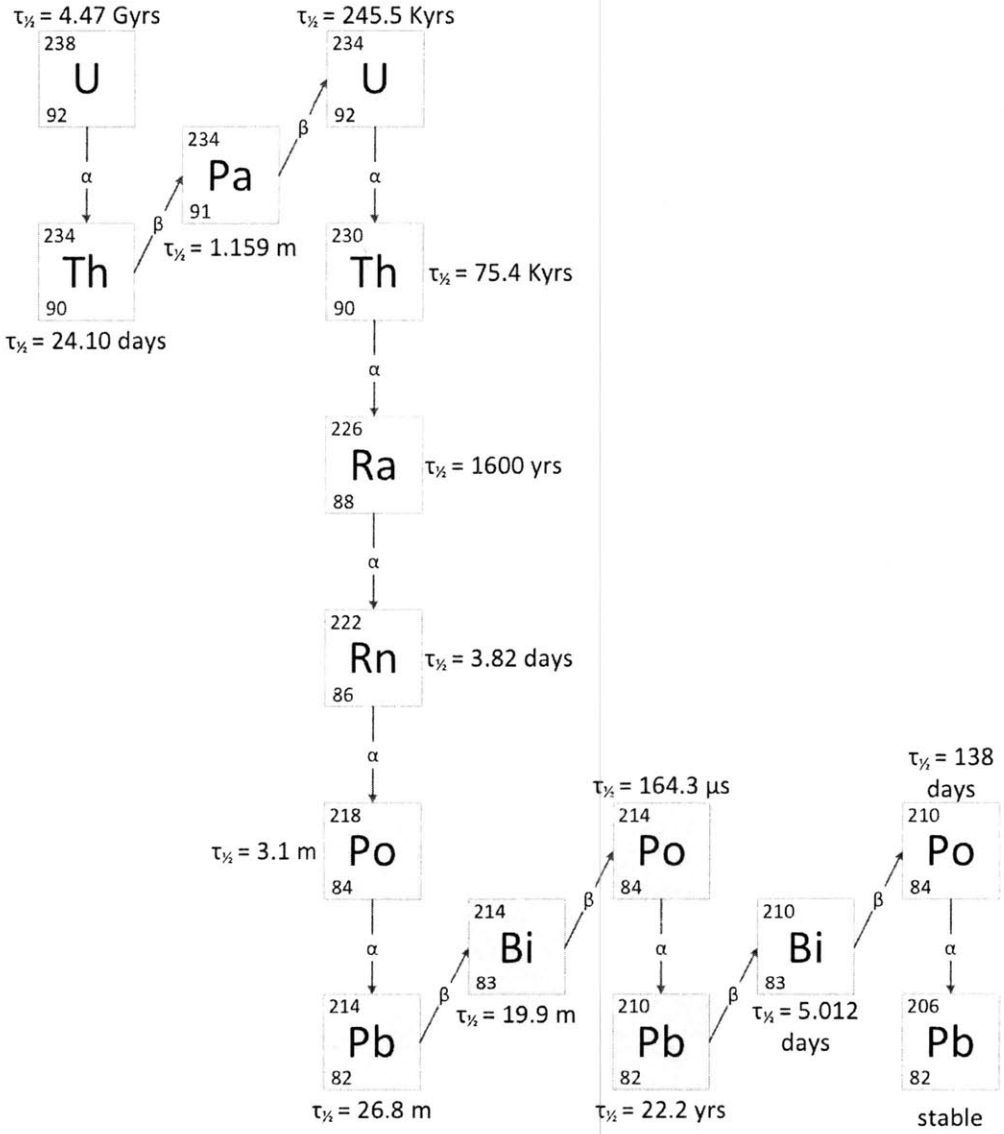

Figure 1-1: The decay chain of ^{222}Rn that originates from ^{238}U. The highlighted daughters are created as positive ions and tend to stick to detector components.

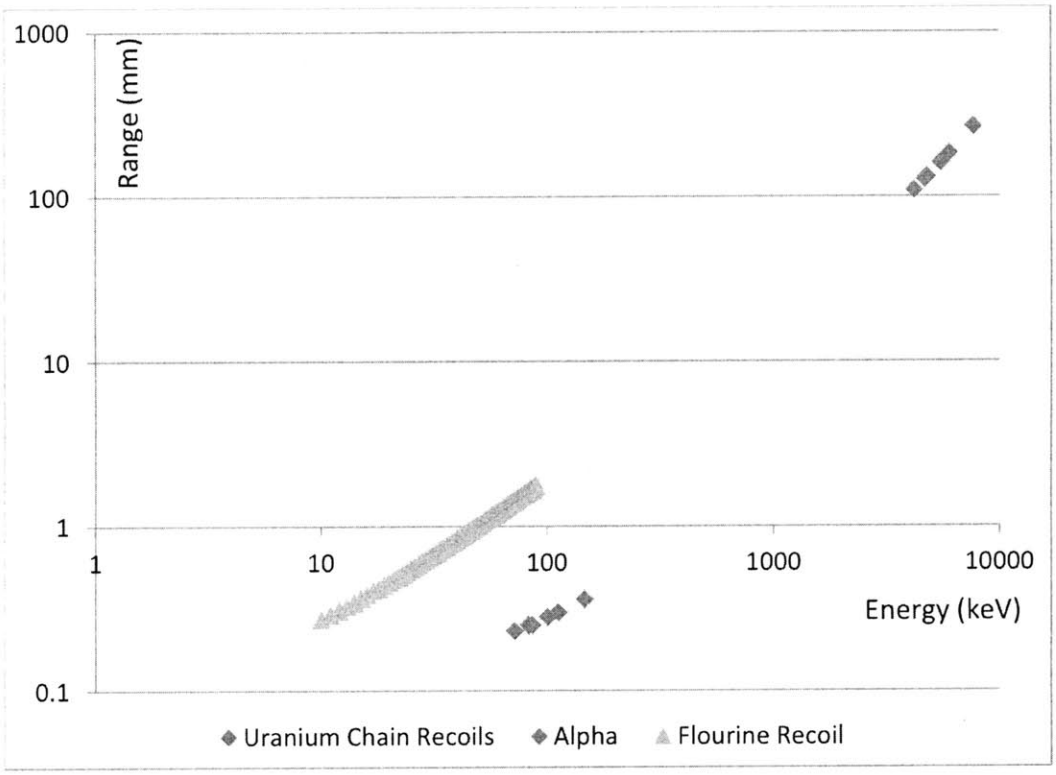

Figure 1-2: Range versus Energy values on a logarithmic plot of uranium chain recoils as well as their respective alpha counterparts. The green streak represents the set of fluorine recoil points, which is realally our range of interest (approx. 10-250 keV). The detector's spatial resolution is approximately 1mm, so anything with a range below 1mm will be indistinguishable.

Table 1.1: List of decays in ^{238}U chain with information on half-life ($T_{1/2}$), Q-value, nuclear recoil energy (E) and range (R), and accompanied alpha energy (E_α) and range (R_α). Recoil ranges are given for 75 Torr of CF_4. WIMP scattering creates signal recoils with range of approximately 1-3 mm and energy 50-150 keV. A chart of the range vs. energy values is provided in Figure 1-2.

Isotope	$T_{1/2}$	Type	Q (keV)	E (keV)	E_α (keV)	R (mm)	R_α (mm)
U-238	4.47E9 y	α	4269.7	71.8	4197.9	0.23	109
Th-234	24.10 d	β	273				
Pa-234	1.159 m	β	2195				
U-234	2.455E5 y	α	4857.7	83	4774.7	0.25	131
Th-230	7.538E4 y	α	4770	83	4687	0.25	127
Ra-226	1600 y	α	4870.6	86.2	4784.4	0.25	131
Rn-222	3.8235 d	α	5590.3	100.7	5489.6	0.28	160
Po-218	3.098 m	α	6114.68	112.2	6002.5	0.30	182
Pb-214	26.8 m	β	1019				
Bi-214	19.9 m	β	3270				
Po-214	164.3 μs	α	7833.46	146.4	7687	0.36	266
Pb-210	22.20 y	β	63.5				
Bi-210	5.012 d	β	1162.1				

Chapter 2

EXPERIMENTAL SETUP

2.1 Operation Principle of the DMTPC Experiment

The Dark Matter Time Projection Chamber (DMTPC) is a particle detector with directional sensitivity. It consists of a certain volume of low-pressure CF_4 gas within a uniform electric field. When a Weakly Interacting Massive Particle (WIMP) passes through the volume it can collide with one of the nuclei in a CF_4 molecule. The nucleus recoils back and ionizes other CF_4 molecules, leaving a trail of primary-ionization electrons. The concept of the detector is illustrated in Figure 2-1.

Under the uniform electric field, the primary-ionization electrons drift toward an amplification gap, which creates an avalanche of electrons with a 10^5 amplification factor. This avalanche of electrons is accompanied by scintillation photons. A CCD overlooking the drift cage then records the photons and reconstructs the track. The sense of the direction (head-tail) of the nuclear recoil can easily be determined because the energy loss varies along the track (See Figure 2-2).

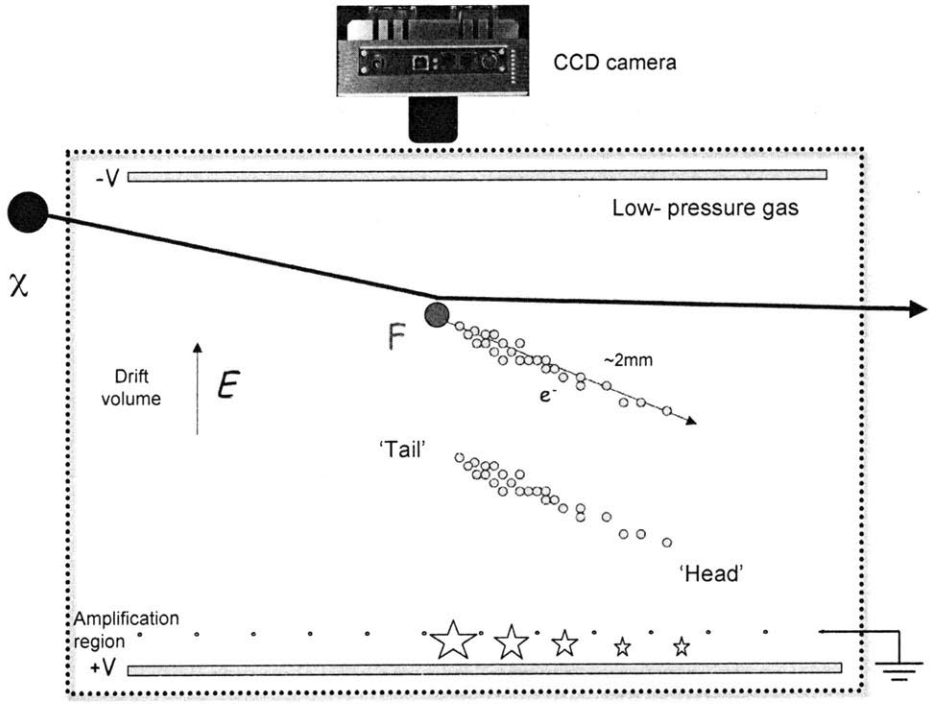

Figure 2-1: A graphic illustrating the general concept of the DMTPC detector. A dark matter particle passing through the sensitive part of the detector collides with a fluorine atom and ionizes it. The recoil also creates an ionization track with a greater density of electrons closer to the impact point. The ionized electrons drift down to the amplification region where they scintillate. A CCD camera on top pick up the light that shows a clearly directional track.

2.2 Canary Detector

The detector, nicknamed "Canary," is a small low-pressure time projection chamber. The vessel is 20L overall, of which 1L is the active detection (fiducial) volume. It has a TPC with micromesh amplification plane [11] and 10 cm drift height. It is equipped with an Andor Luca EMCCD camera or Apogee U6 CCD camera for optical readout. For charge readout of the central anode, we use a Cremat CR-113 charge-sensitive pre-amplifier that has a gain of 1.5 mV/pC. The outer anode ("veto") uses CR-112 that has a gain of 15mV/pC. (See Figure 2-3)

The TPC has standard 0.44 mm spacers at a 2.5 cm pitch. The amplification mesh is composed of 28 μm stainless steel wires at 256 μm pitch; the drift mesh is composed of 30 μm stainless steel wire at a 512 μm pitch. It is pictured in Figure 2-4. The anode voltage is set at +720V and the drift cathode voltage at -1500V. The TPC is also surrounded by a drift cage that will be discussed in more detail in section 2.3.

The Apogee U6 comes with a Kodak Grade 2 KAF-1001E (1024 X 1024 pixel array) full-frame sensor with high quantum efficiency, low dark current, and high full well capacity. The CCD is operated at a $-20°C$ temperature and with 4x4 binning. The gain is approximately 10ADU/keV, and the noise is 7 ADU/keV. The lens is a Nikon 55mm/1.2, and the viewfield is 16x16cm^2.

The EMCCD is an Andor Luca Luc285_MONO model with a 1000x1000 pixel resolution and readout using 8x8 binning. The CCD is maintained at a $-20°C$ temperature and the total gain (TPC plus EMCCD) is 200 ADU/keV, and noise is 300ADU/keV. The lens is a Scheider 25mm/0.25, and the camera viewfield is limited to a square 10.7cm wide by 10.7cm long around the center of the TPC. (See picture 2-5).

An EMCCD is an Electron Multiplying Charge Coupled Device, which uses impact ionization to multiply the number of electrons per photon, thus increasing the gain of the CCD. EMCCDs are especially suited for very low-light applications, where noise-to-signal ration is quite drastic. Because each signal yields many thousands of electrons, the readout noise - typically a few electrons - becomes negligible. The

experiments used different cameras as they became available. The Andor Luca EM-CCD was used for the α rate calculation, and the Apogee was used for α energy measurements.

Before every set of runs the detector is pumped down to a near vacuum ($\sim$ 0.001Torr), and then filled with pure CF_4 gas up to 75Torr. All valves are then closed, voltages set, and the camera set to take 3600 pictures with 5-sec exposures. The exposure is set to 5 seconds because it yields a noise level of approximately 300/bin. This has been found to be the best balance between long exposure and low noise.

2.3 Drift Cage

The sensitive part of the detector is surrounded by a series of rings interconnected by 1.3MΩ resistors (Figure 2-6). The bottommost ring is connected to the grounded mesh with a separation of 6mm. Similarly, the topmost ring is connected to the anode mesh with similar separation. Further specifications of the canary detector drift cage are given in Table 2.1.

The main purpose of the drift cage is to maintain a uniform electric field within the sensitive area of the detector to minimize sideways drifting of electrons. Such sideways drifting can distort the shape or location of the signal.

The current ring design of the drift cage was adopted after numerous simulations and prototypes proved the ring method to be the most uniform field with the minimum number of rings. Results of the calculation are shown later on in this chapter.

Parameter	Value
Number of Rings	13
Outside Diameter	31.5cm
Inside Diameter	26.5cm
Pitch (center to center)	8mm
Ring Thickness	2mm
Distance to Mesh	6mm
Cathode Voltage	-2500V

Table 2.1: A list of Canary drift cage components

In order to model the geometry of our drift cage, a 2D cross-section across the middle of the drift cage has been taken. Thus, all the circular rings are modeled as small rectangles at either end. The cathode and ground meshes, then, are modeled as thin rectangles spanning the entire width of the drift cage.

Figure 2-8 shows our model with an overlaid coordinate system. The model is inverted for working convenience, and this inversion doesn't affect the results, since the drift cage is symmetric. A plot of the model with the Finite Elements Method (FEM: see Appendix A) meshing can be seen in Figure 2-7.

In order to explore the quality of the drift cage, the uniformity of the electric field must be examined. A plot of the model's electric potential isolines is provided in Figure 2-8. The lines look mostly parallel, except near the rings. To visualize these fringe fields better, a plot of the transverse electric differential ($|E_x/E|$) is provided in Figure 2-9. The color scale in the isoline figure shows the voltage values around the rings (the color of the rings themselves is arbitrary and unimportant), which decrease going up (or, in the real drift cage, going down - due to resistors attached between the rings). The color scale in the transverse graph shows the strength of the transverse electric field compared to the total field. Anything green, which is around the edges, is bound to be problematic. As will be discussed below, this is fortunately not a concern for the present DMTPC

It is also possible to observe the effect of these fringe fields. To this extent, a simulated point charge is dropped anywhere within the drift cage model and allowed to follow the FEM-generated field lines until it hits the amplification plane (the long red rectangle at the top of all model figures). Its ρ coordinate difference can then be measured to show how much it has moved toward the center.

This has been done for a set of points successively further from the center at three different heights. Electrons that are drifting from a low Z height are not disturbed by fringe fields. However, electrons drifting from a 10cm height are shifted about 2.5mm toward the center. This result is also shown in Figure 2-10. Taking into account physical diffusion effects and the resolution of the detector, it would be a safe estimate to state that charge diffusion should not exceed 0.4 mm. At this value, it is

advisable to limit the effective viewfield to no more than a 12 cm radius.

In the current detector, the edges of the drift cage are not imaged (see Figure 2-5 for an understanding of the current viewfield). This means that the charge shift for larger ρ is not a problem. The newer version of DMTPC, however, will image the entire cage, and this may be prone to problems. Caution must be exercised and it may be necessary to cut out events that are too close to the edges in addition to any that cross the edges anyway.

For the current DMTPC detector, images and charge waveforms are recorded for every exposure. Events are later analyzed and those with alpha tracks are selected, whereas others with sparks or no tracks are rejected.

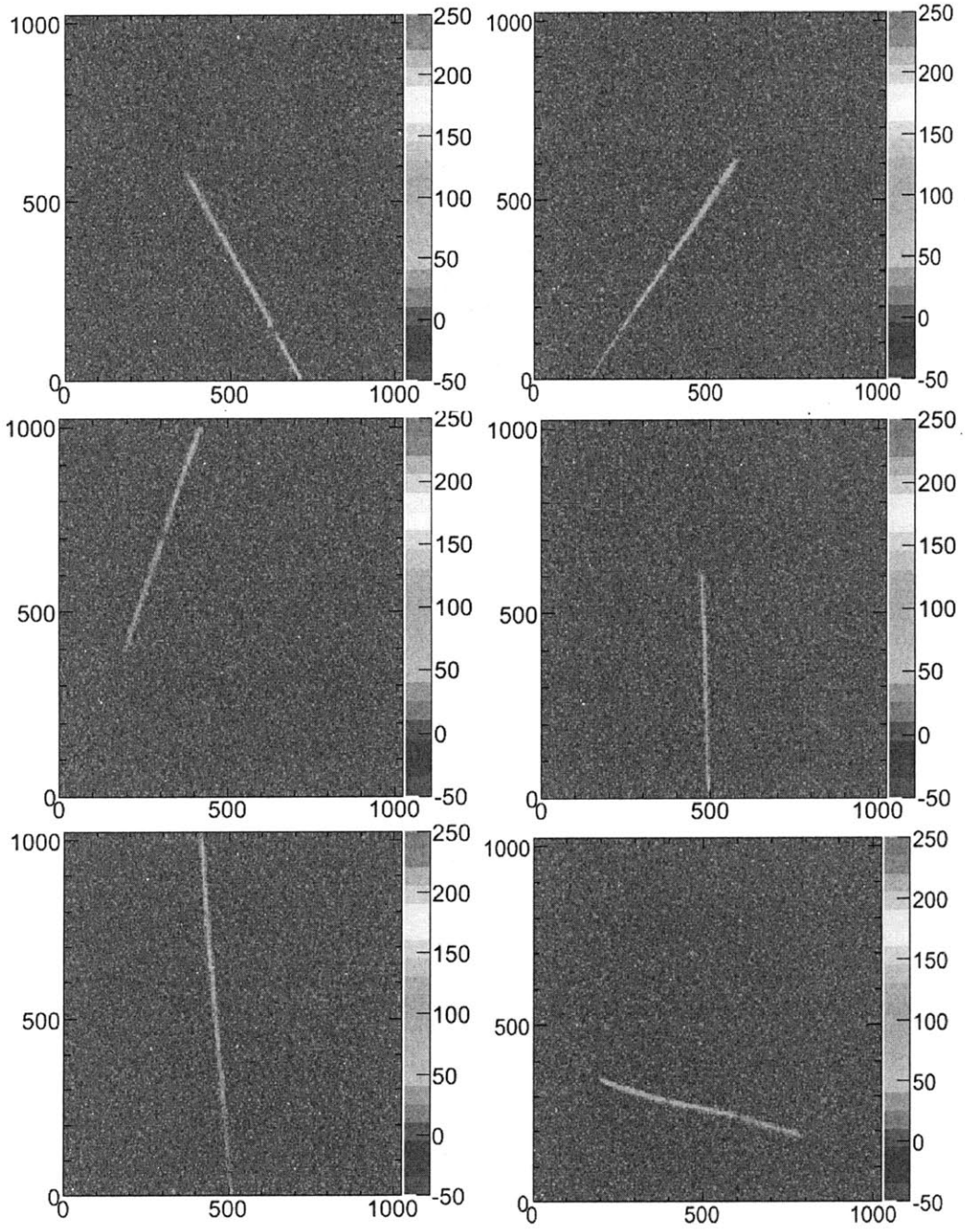

Figure 2-2: Examples of background alpha events. You may notice that it is easy to see the sense of the direction in most of them (specifically the bottom-left example by how the track is thicker at the top and thinner at the bottom). Colors represent the pixel intensity in analog-to-digital units (ADU's). The bottom-right image shows a track that does not touch the boundary. This signifies that the alpha came from inside the detector, most probably from a radon chain decay. These are the types of events that are of particular interest.

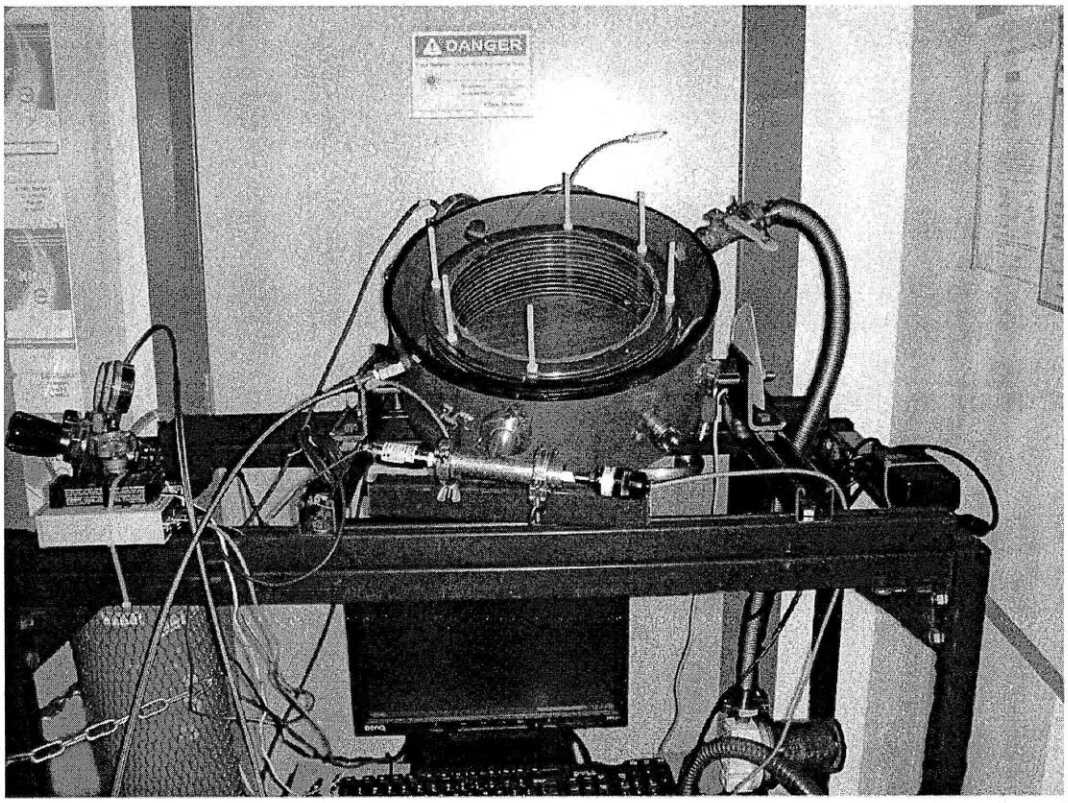

Figure 2-3: A picture of the Canary Detector with its top portion (lid+camera) removed to expose the Drift Cage

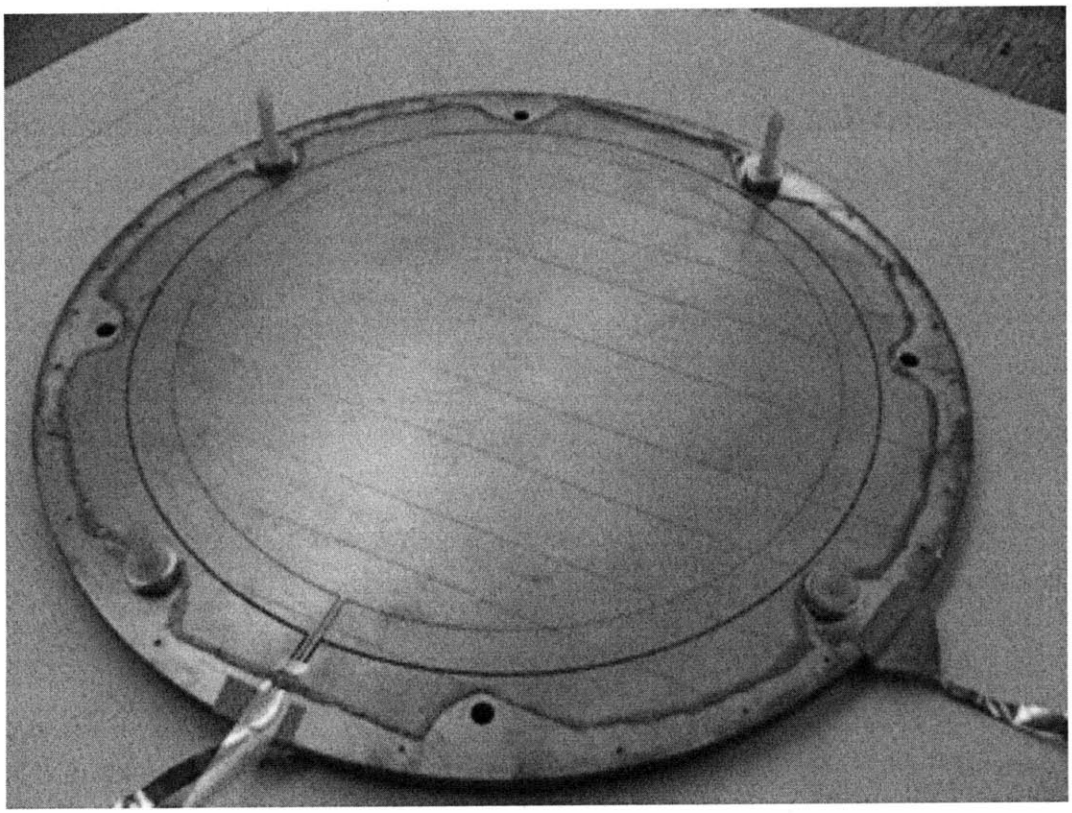

Figure 2-4: The amplification plane with the mesh stretched out on the top, and the copper anode plate supporting it at the bottom. This picture also shows the separation between the inner (central) anode and the outer (veto) anode.

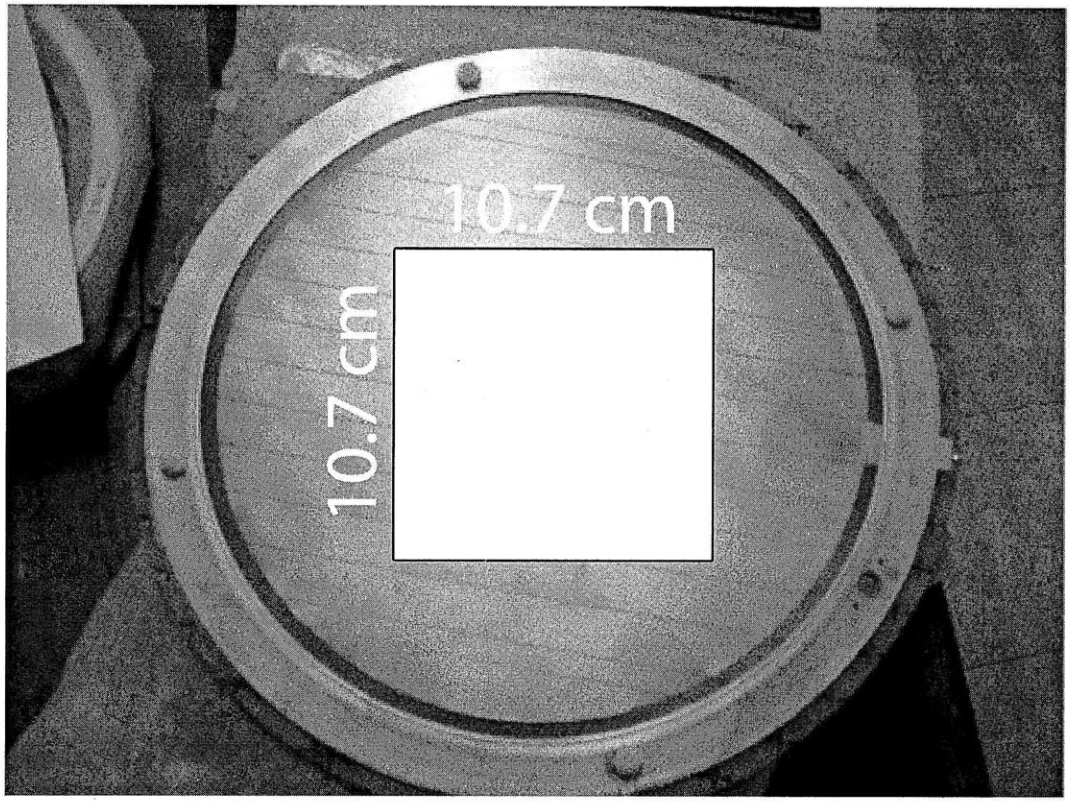

Figure 2-5: A top-down view of the TPC and the Drift Cage with the approximate camera viewfield marked.

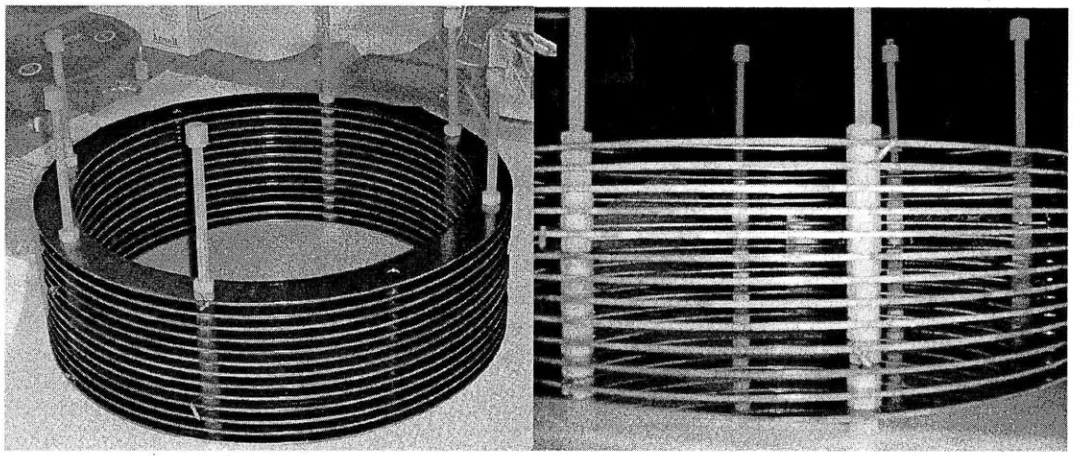

Figure 2-6: Two views of the copper ring drift cage

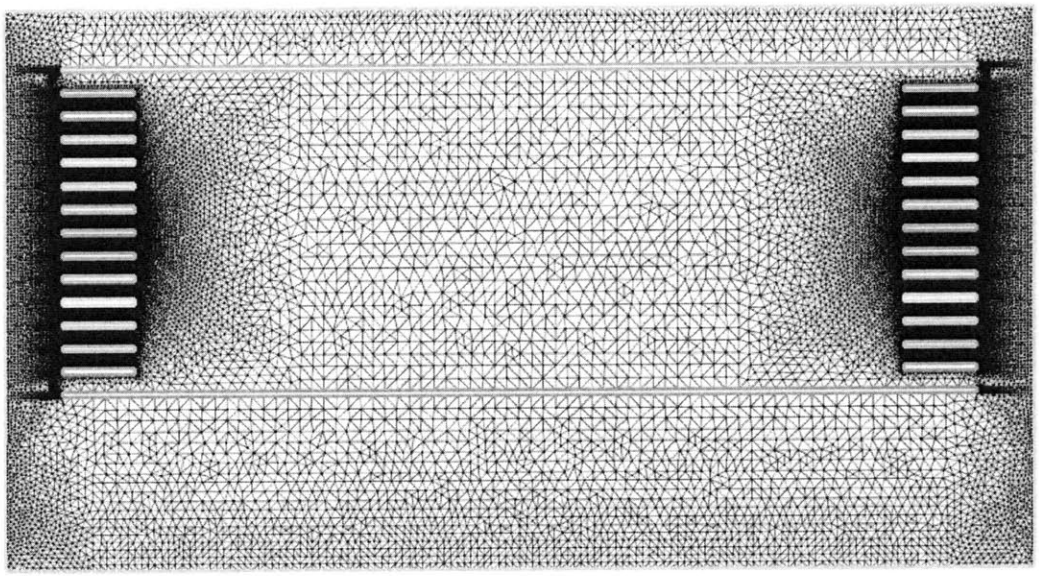

Figure 2-7: The mesh created by the Finite Elements Method to calculate electric potential and field values within the canary drift cage. The closer an area is to a known point (contributing source) of electric field, the denser the nodes.

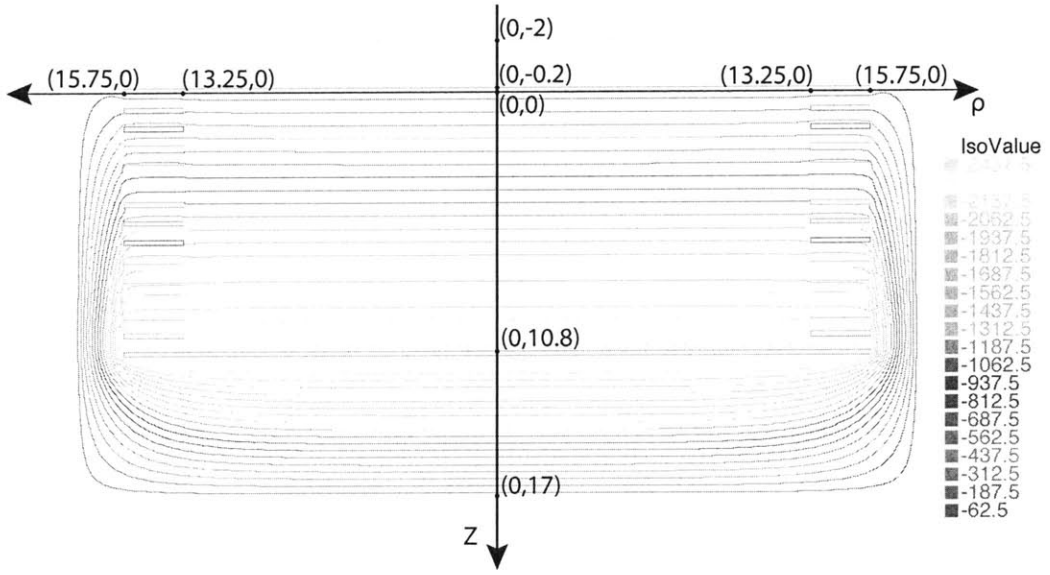

Figure 2-8: Plot of the isolines with an overlay of a cylindrical coordinate system. As mentioned, the model is an upside-down representation of the actual cage with the cathode in the model's bottom (as opposed to the top). The drift cage itself is 11.2 cm from bottom of one mesh to the top of the other, and spans a total of 31.5 cm in width

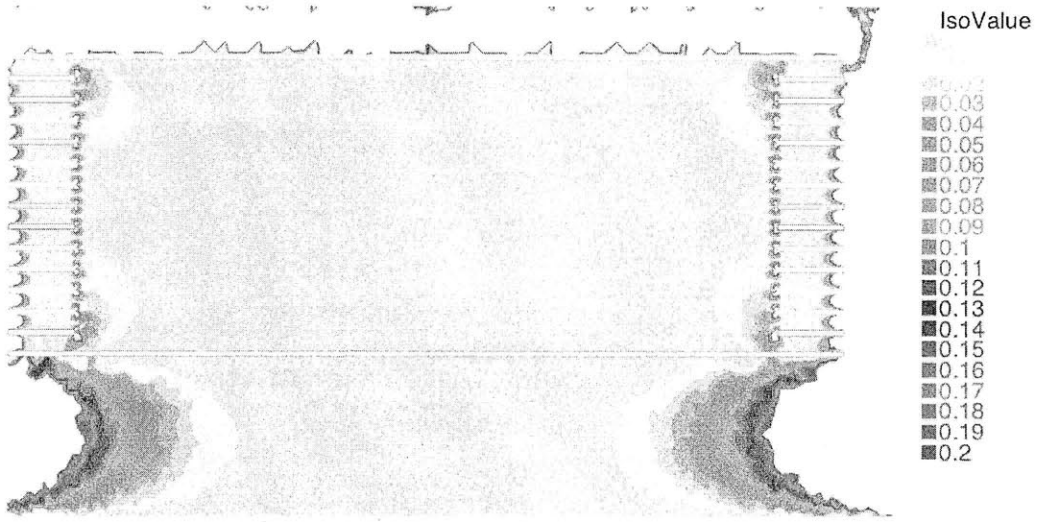

Figure 2-9: Plot of the differential of transverse electric field ($|E_x/E|$). The plot is both vertically and horizontally symmetric around the center axes of the drift cage.

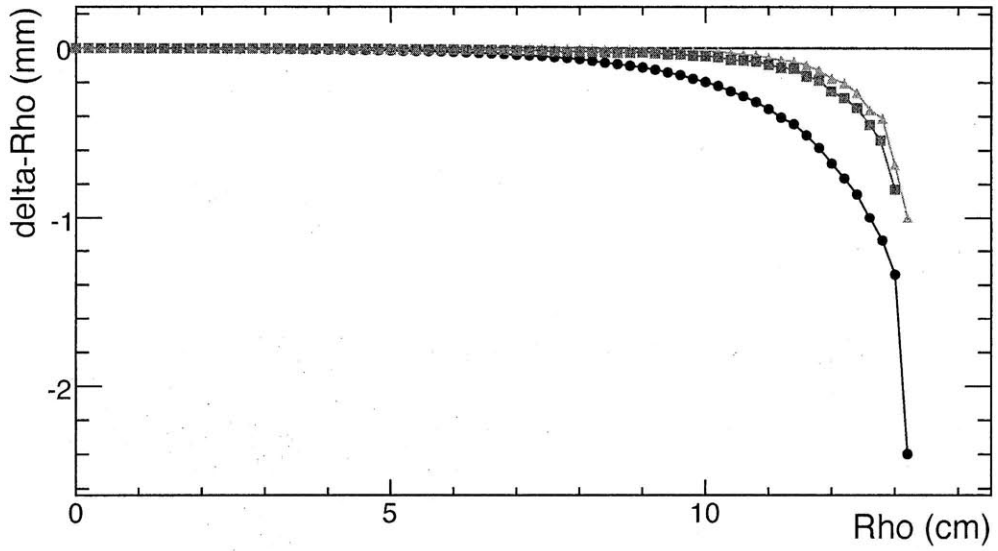

Figure 2-10: Plot of the radial deflection of electrons due solely to fringe fields. The red triangles indicate a height of z=9.8 cm from the amplification plane (see Figure 2-8 for dimensions). The black circles indicate a height of z=5.4 cm (halfway up) from the amplification plane, and the blue squares a height of z=1 cm. The inner radius of the model (i.e. distance to ring) is 13.25 cm.

Chapter 3

ENERGY SPECTRUM OF ALPHA BACKGROUND

3.1 Energy Calibration

The Canary TPC is calibrated using an alpha source (^{241}Am) that has well-defined kinetic energy (5.486 MeV). However, the source is covered with a window of unknown thickness and composition so the energy of alphas exiting the source is not known a priori.

A calibration is performed in two steps. In the first step the ^{241}Am alpha source is calibrated by comparing alpha energies from ^{241}Am source with alphas from a source emitting ^{222}Rn gas. This is done in a smaller vessel under vacuum and using a surface barrier detector. This feature was used to calibrate all alpha sources that have been used in the DMTPC project.

In the second step the calibrated ^{241}Am is used to measure response in Canary TPC detector.

3.1.1 Energy Calibration of ^{241}Am Source

An ^{241}Am alpha source is housed in the same chamber as the surface barrier detector (Canberra 450-20AM), approximatelly 2 cm from the detector in a position where

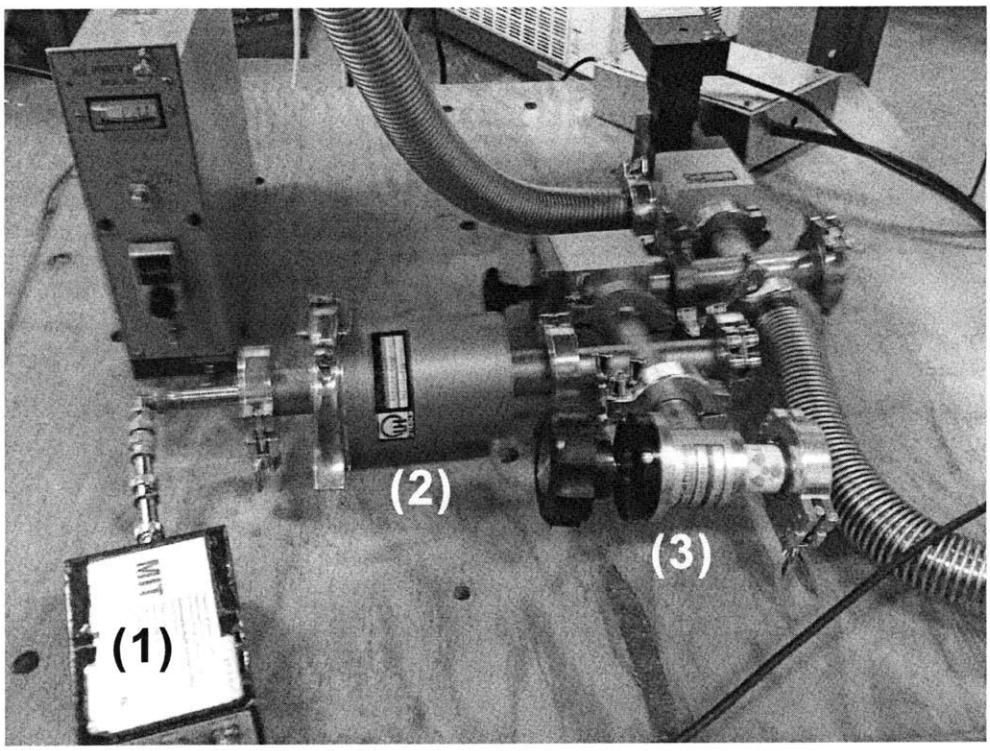

Figure 3-1: Actual setup of the source calibration. Preamplifier is on the bottom left (1), connected directly to a chamber housing the surface barrier detector and the alpha source (2). The radon is produced by the uranite rock stored in the bottom right chamber (3).

a collimated beam of alphas strikes at the approximate center of the detector. The uranite rock is used for radon generation, and is enclosed in a separate chamber with a valve control. All measurements are made in vacuum. Signals generated in the detector are processed with a preamplifier (Canberra 2004) and an amplifier (Ortec 855) before being sent to the digitizer (Alazar ATS860). A photo of the setup can be found in Figure 3-1. A simplified diagram can be seen in Figure 3-2.

Several pre-calibration runs are done with radon only (no alpha source). The goal is to have precise measurements for radon by itself to calibrate any alpha source that will later be put into the detector. However, it is found that radon energy value measurements do not always agree. This can be seen in Figure 3-3. This disagreement is due to several factors, including detector gain change after power-off, radon density, vacuum efficiency and outgassing. However, the value tends to stabilize over time to

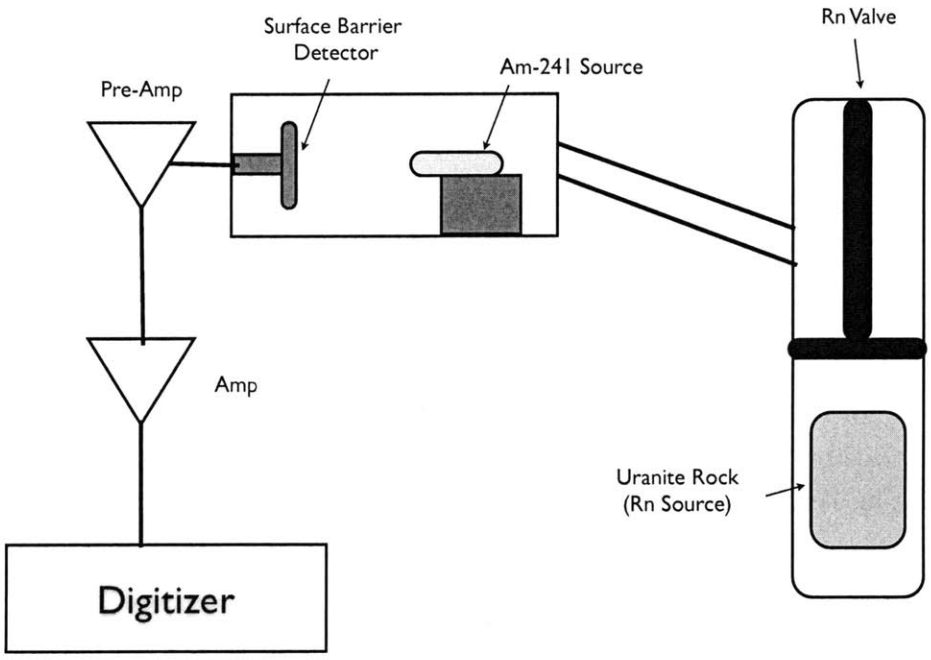

Figure 3-2: Simplified diagram of the source calibration setup.

Table 3.1: Alpha Source Energies. Sources C and E are used for DMTPC surface runs. Error is approx. 1%. Source E is used in this work and calibration of Canary TPC.

Source	Peak Energy (MeV)
Am-241 B	4.44
Am-241 C	4.51
Am-241 E	4.44

the same constant regardless of the run.

To correct for this problem, it was decided to take the radon and alpha source measurements together. The scatter plot of mean event values in Figure 3-4 shows that the measured values are stable within the 1.4 hour period of each 1000 five-second exposure run.

A typical run would produce an aggregate image such as the one shown in Figure 3-5, where the largest of the four peaks corresponds to the alpha source, and the other three to radon and its progeny. Since the physical energy values of the latter are well known, it is possible to extrapolate the energy value of the alpha particle using the means of these aggregated values.

Thus, taking the mean of the gaussian spread of charge readout (voltage) values of radon and the two polonium alphas, we end up with specific channel values for each of the three. Their energy values can easily be calculated from the Q-values provided in Table 1.1 through a simple energy conservation equation. Equating the two sets of values, we can end up with a linear function like the one in Figure 3-6. With this function, one can extrapolate the energy of the alpha sources. The values for the alpha sources used in the DMTPC experiment are provided in Table 3.1.

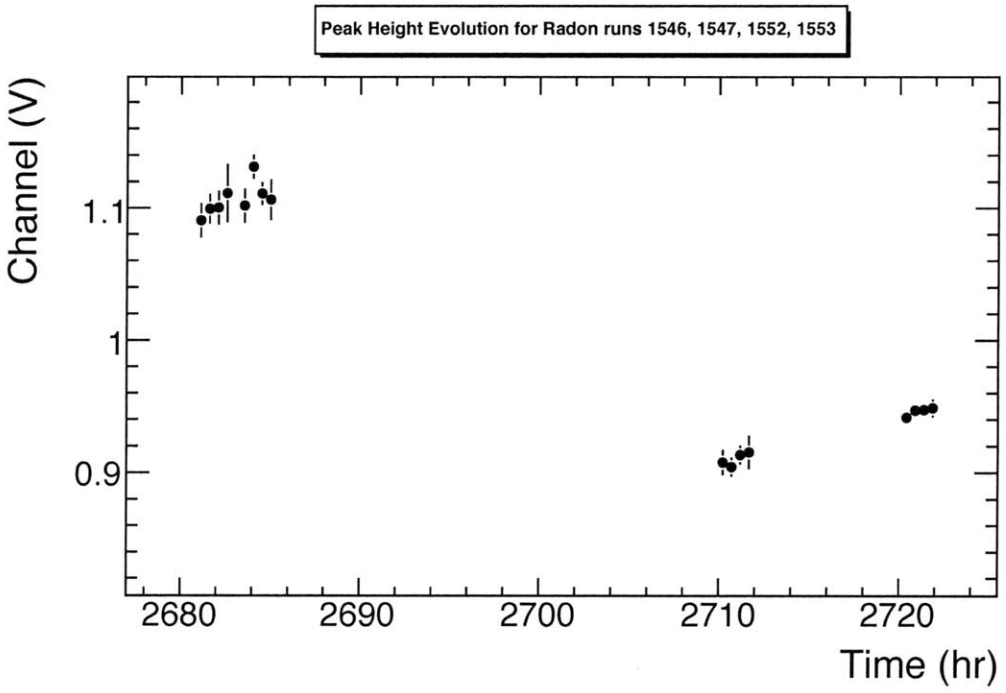

Figure 3-3: Radon alpha energy measurement instability. The points are measurements of the mean of the radon alpha energy in the digitzer (measured in volts). Each cluster of events is a set of runs. All three runs disagree by a significant amount. This disagreement is a result of changes in gain between runs. As mentioned earlier, this problem doesn't persist and the values stabilize.

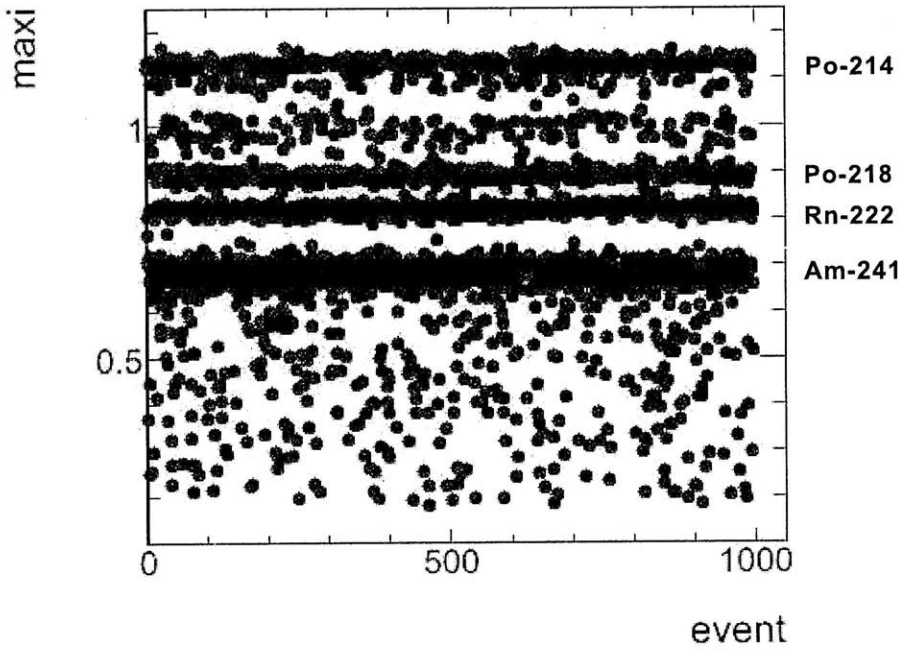

Figure 3-4: Plot of signal heights in the detector versus the number of the 5-sec exposure frame. The Y-coordinate values are in Volts. The band of points just above 0.6V corresponds to the Am-241 alpha source, and the three thick bands above it are, respectively, Rn-222, Po-218, and Po-214. The fact that these bands stay parallel to the X-axis shows that values are stable within each run.

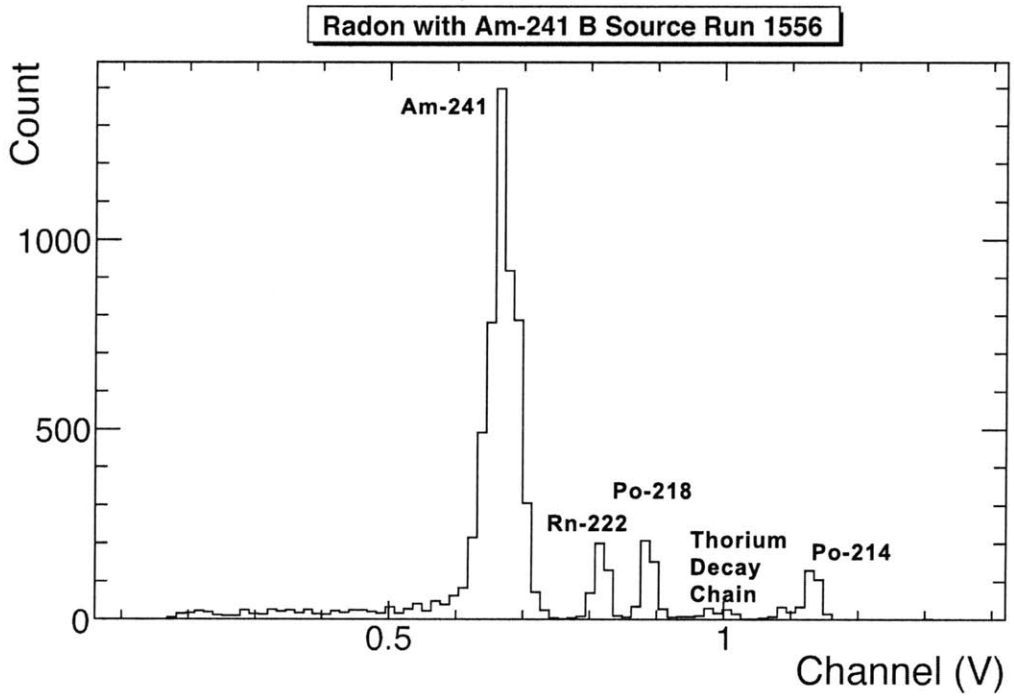

Figure 3-5: Histogram of alpha energy measurements. These charge readouts are aggregations of single-pulse events registered in the digitizer (for more information on the digitizer, see Section 3.1.1). The four peaks, from left to right are: Am-241, Rn-222, Po-218, and Po-214. The miniscule peaks between the two Polonium peaks are caused by other radioactive nuclei in the thorium chain.

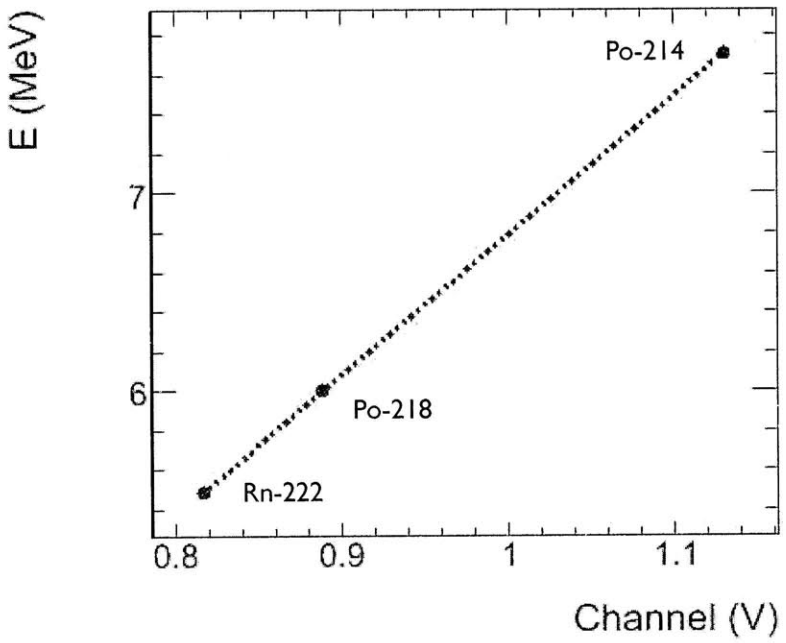

Figure 3-6: Linear fit to the channel values of radon and its progeny, taken by the surface barrier detector. This function can be used to extrapolate the energies of alpha sources with known channel values in the same run.

3.1.2 Energy Calibration of Canary TPC

A calibratied ^{241}Am source is placed in a Canary TPC such that the total energy is deposited in the viewfied of a CCD camera and the entire charge is collected by the central anode. An event with an alpha track is shown in Figure 3-7.

A typical CCD image is shown in the top plot of Figure 3-7. The energy of an alpha track in a CCD image is computed from the total light intensity after background subtraction.

The central anode is read out with a preamplifier (CR-113) that gives approximately 1.5 mV/pC, and the outer anode uses a different preamplifier (CR-112) that has a sensitivity of 15 mV/pC. Therefore, the signal amplitude on the outer anode should be scaled by a factor of 10 in order to be comparable. Typical responses to an alpha track are shown in the two bottom plots in Figure 3-7. The energy of a track is reconstructed as the peak height in the recorded waveform of the inner anode.

Energy responses from roughly two thousand alpha tracks are accumulated and plotted in Figure 3-8. Peak positions correspond to energy of alpha source (E) given in Table 3.1. Energy calibration factors for the CCD and charge readout are listed in Table 3.2.

Readout	Constant
CCD	$4.44/24100 = 1.83\ 10^{-4}$ MeV/ADU
Charge	$4.44/0.71 = 6.20$ MeV/V

Table 3.2: Energy calibration constants for source ^{241}Am E.

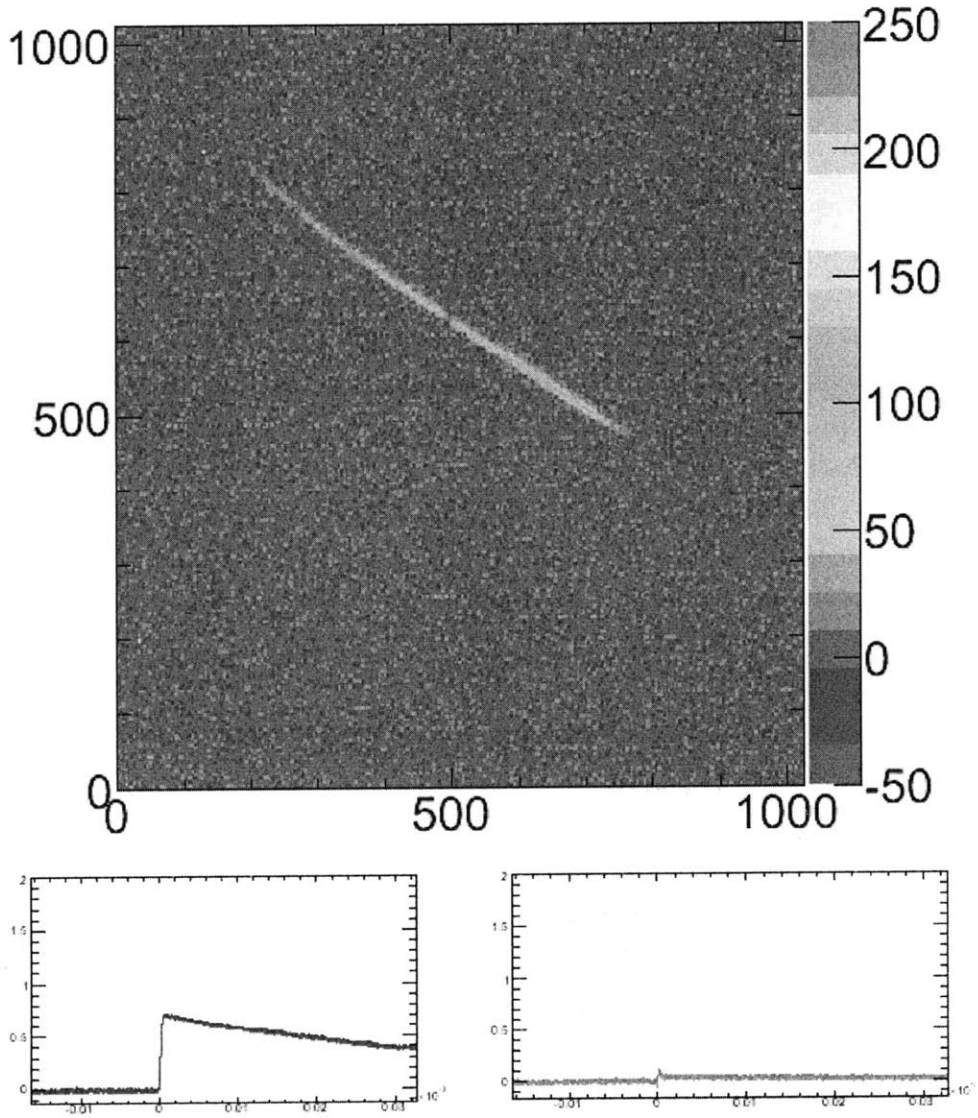

Figure 3-7: An alpha track recorded with a CCD camera (top) and charge readout of the anode (bottom). The waveform on the left shows the total collected charge on the inner anode, and the waveform on the right shows the charge collected on the outer anode. The inner anode collects the total charge while the outer waveform is consistent with a noise for fully contained alpha particles.

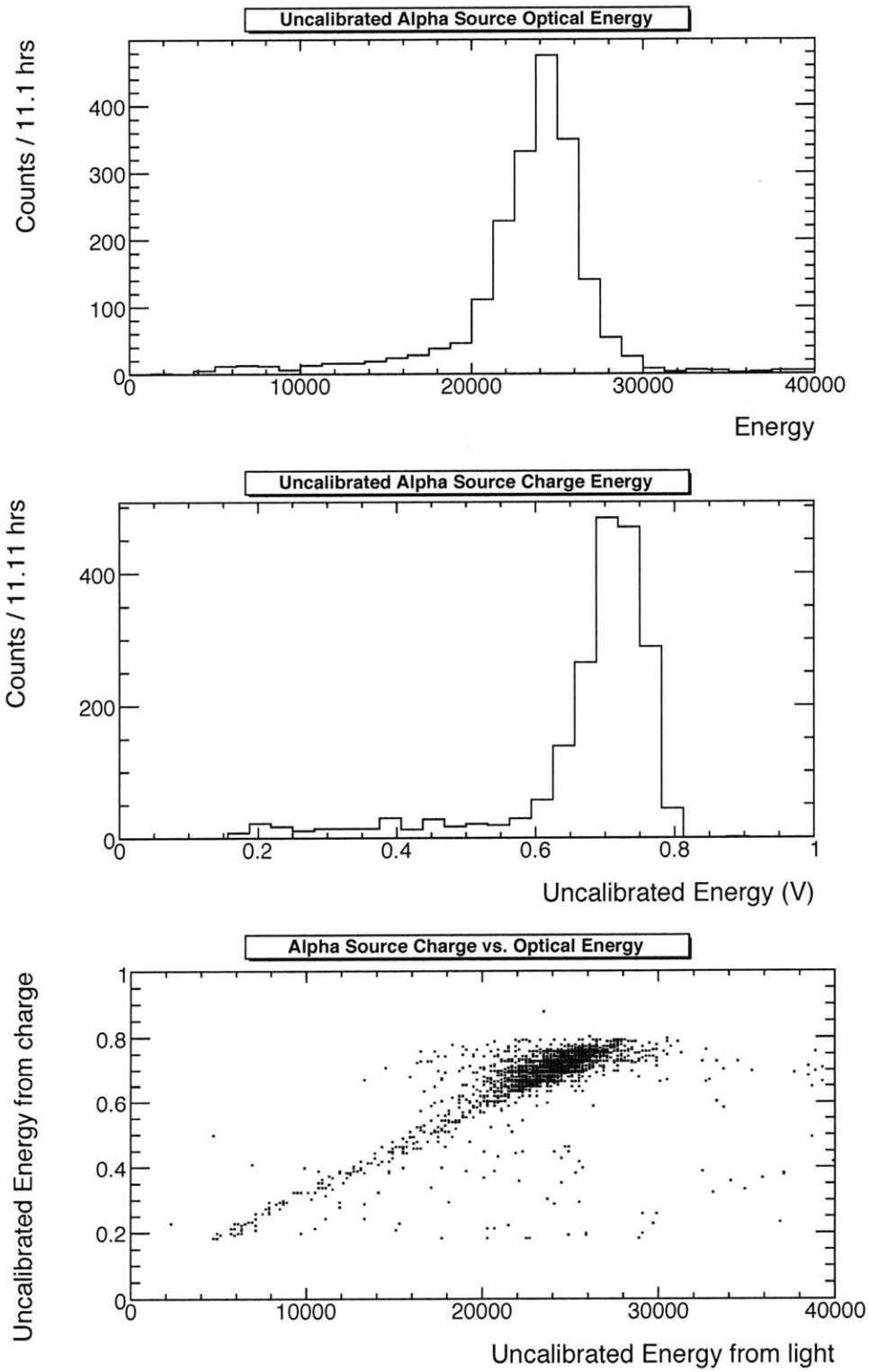

Figure 3-8: Distribution of alpha particle energies. The peaks correspond to 4.44 MeV of deposited energy in CCD (top), inner anode (middle), and a comparison between CCD and charge signals (bottom).

3.2 Energy of Alpha Background

After the energy calibration with the ^{241}Am source, the Canary TPC is left to run for approximately 50 hours without any alpha sources inside. All the signals from both the charge and CCD readouts are aggregated to show signs of accumulation of other alpha-releasing agents.The results, as can be seen in Figure 3-9, show a very low level of background (~20 counts per 47 hours, during which the gain was constant to about 1%).

Using the data from the alpha calibration, the raw optical yield and charge readout voltage values are calibrated to MeV units. This helps us conclude that there is a clear predominance of signals in the 4-6 MeV range. We claim that this is not radon, but earlier decays in the chain. If radon and its daughters were predominant, we would see decays around 7.7 MeV (see Figure 3-5).

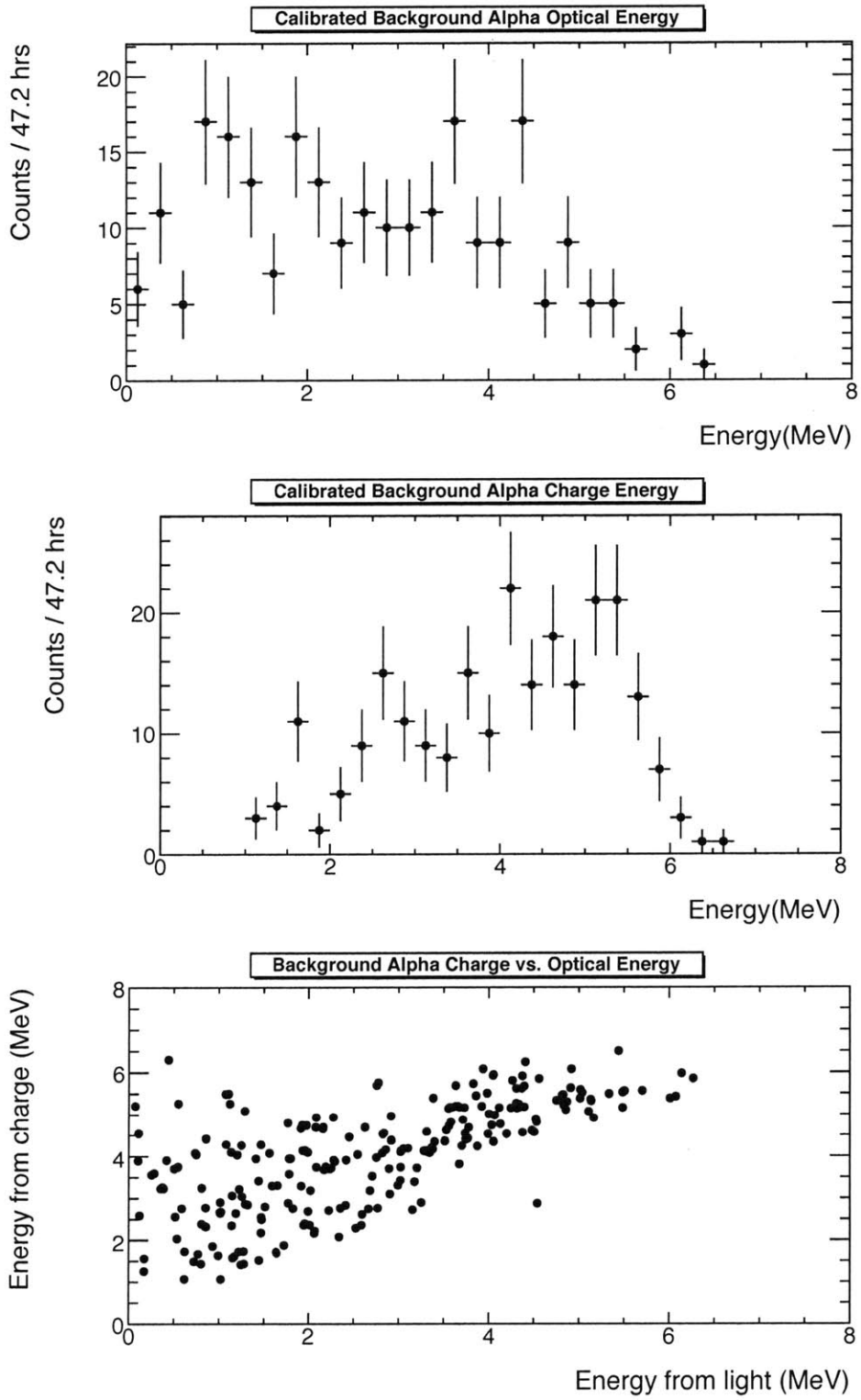

Figure 3-9: Distribution of background alpha particle energies. The main peaks correspond to deposited energy from the thorium decay chain. The plots show energy deposition in CCD (top), inner anode (middle), and a comparison between CCD and charge signals (bottom). All energy values have been calibrated using the values in Table 3.2. The minor discrepancies between the optical and charge readout values, especially in the lower half of the energy spectrum, are due to the corner effects of the rectangular shape of the viewfield.

Chapter 4

RATE OF ALPHA BACKGROUND

The rate of the alpha background coming from radon decay has been of interest to several other experiments, including DRIFT [9] and NEWAGE [10]. To parametrize the decay rate of radon, DRIFT used a modification on the Bateman's equation, which looks at the half-life of the parent nucleus as well as the rate of gas flow through the detector [9]:

$$R(t) = \frac{\kappa}{(1+\frac{\tau}{\rho})}(1 - e^{-t/\tau} - e^{-t/\rho}), \tag{4.1}$$

where R is the rate at which event decays occur, τ is the ^{222}Rn lifetime, ρ is the $1/e$ flush time for the system, and κ is the constant rate at which events are supplied. The κ is then set according to a fitting of the data. The results acquired by DRIFT can be seen in Figure 4-1. The characteristic rise in the rate is due to radon buildup into the DRIFT detector. A similar result has been seen in NEWAGE [10].

The important question, then, is what the true profile of alpha background is in the DMTPC, and whether radon buildup is as big a problem for DMTPC as it is for other experiments.

To analyze this problem, several runs were made with the detector. After obtaining the batch of images from the CCD, a Hough transform (see Appendix B)

algorithm was used to find tracks. All sparks and empty events were eliminated from the batch but accounted for in total exposure calculations. After it was confirmed that the rate is stable with time using an α source, all event images were used to normalize the rate to 5 second exposures. The results are shown in Figure 4-2.

Initially (see Figure 4-2), the Canary detector, outfitted with stainless steel rings, was artificially filled with some radon for calibration purposes. Within 4-5 days, the alpha levels decayed to a stable level (around 900 hrs). The stainless steel rings were then replaced by copper rings, and the alpha rate reduced five-fold. This drop is pictured in Figure 4-3. We thus conclude that the majority of the alpha background has been coming from the uranium and thorium in the stainless steel rings.

Looking back at Figure 4-2, the next step was to introduce a copper shielding around the drift cage inside the detector. This would effectively block any alphas coming from the outside or from the inside wall of the vacuum vessel (also made of stainless steel). Figure 4-4 shows that the change in the alpha rate, if any, is negligible. This effectively disfavors the idea that radon could be leaking or outgassing into the detector. Most importantly, alpha rate stayed constant in time and decreased only when the stainless steel rings were replaced by copper rings.

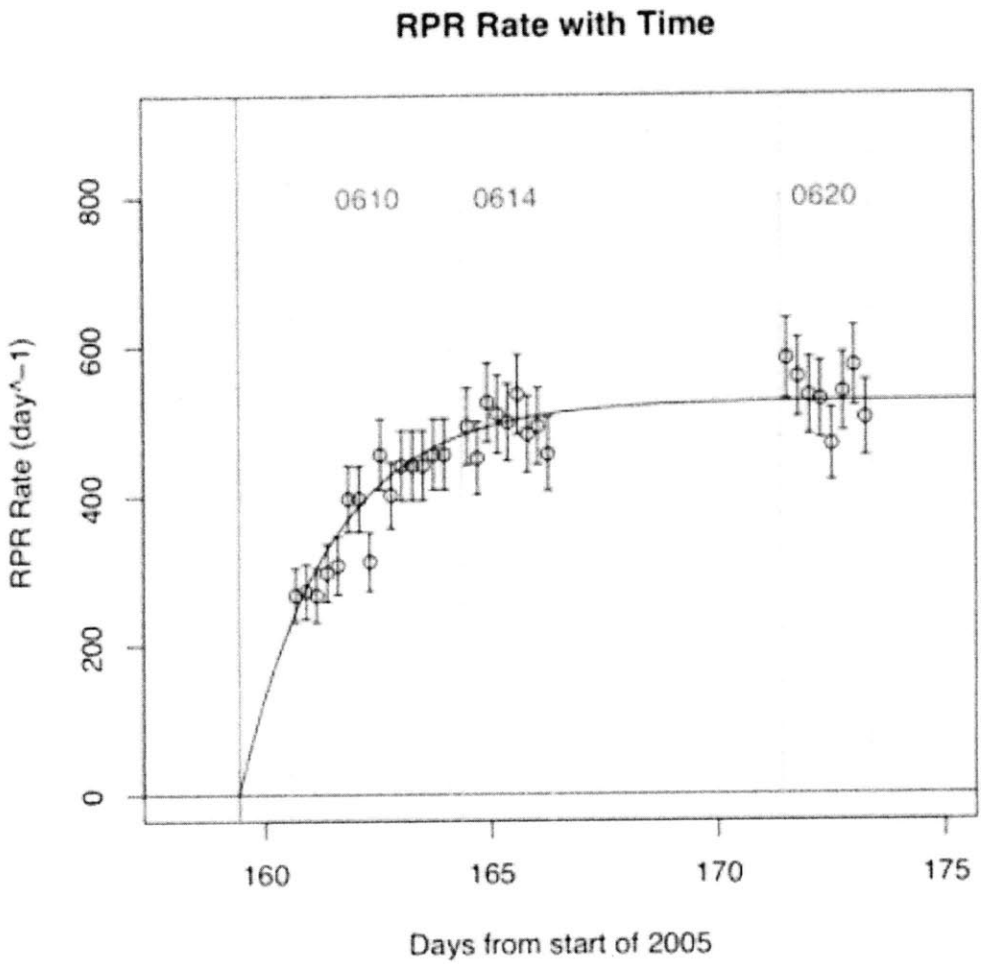

Figure 4-1: From the DRIFT paper [9]: "This plot shows the rate of RPR events as a function of time. The red numbers are file designators corresponding to the date when the run started. The red line shows the time at which the evacuated vacuum vessel was filled with CS_2. Shortly thereafter runs were started. The fit for this plot indicates $\kappa = (1450 \pm 175) day^{-1}$ with a reduced chi-squared of 0.55." The rate increase seen in the DRIFT detector is due to radon building up.

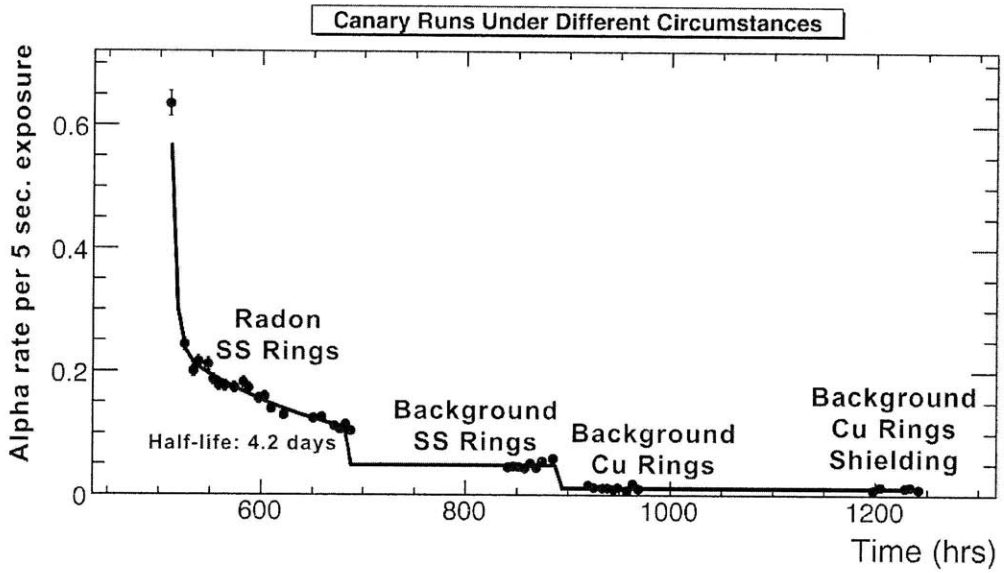

Figure 4-2: Plot of alpha activity per each 5 second exposure in the Canary chamber throughout time. The graphic shows the alpha activity level within the chamber in four different scenarios. The initial exponential decay is due to radon being artificially pumped into the detector in order to verify the predominance of radon through a half-life calculation. The replacement of the stainless steel rings by purified copper rings has had a huge effect on reducing background. At the same time, shielding of the drift cage from the rest of the chamber by a copper sheet seems to be ineffective. More detailed comparisons are given in Figures 4-3 and 4-4.

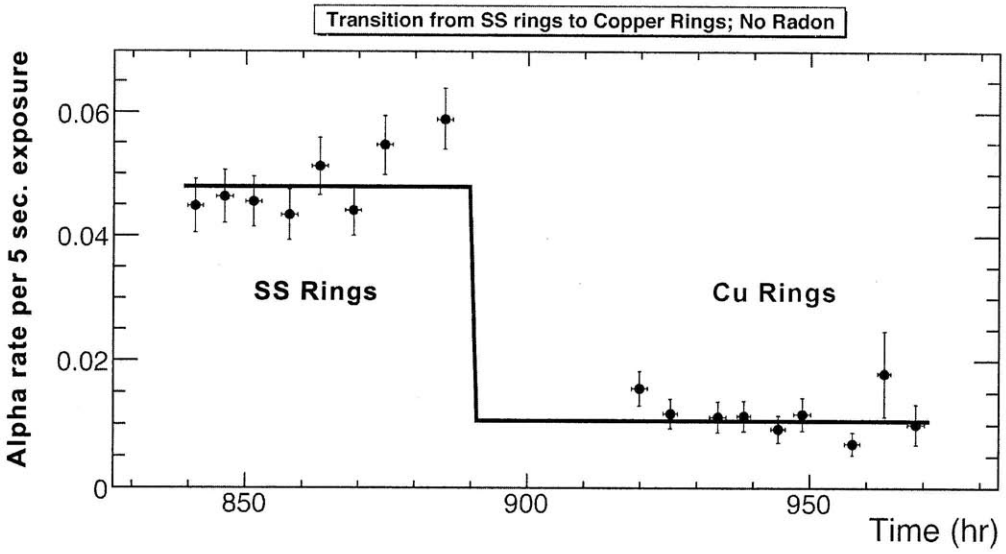

Figure 4-3: Plot of alpha activity in the Canary chamber with stainless steel and Copper drift cage rings. The plot clearly shows a decrease in alpha background after the change. The high background with the SS rings is most likely due to the decay chain of uranium and thorium that are present in trace amounts in the stainless steel.

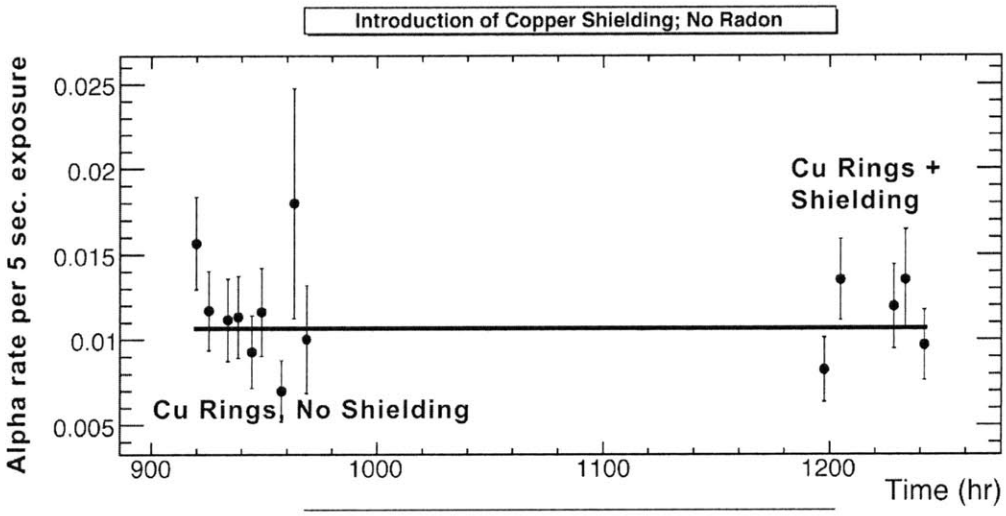

Figure 4-4: Plot of alpha activity in the Canary chamber throughout time before and after the installation of a copper shield outside and around the drift cage. There is no significant decrease in alpha background in the chamber after the installation of the shielding. This means that the effect of radon outgassing or leaking into the chamber is negligible, and the main contributors of alpha background are uranium and thorium decay chain daughters from inside of the drift cage.

Chapter 5

SUMMARY

The purpose of the research was to determine the source of α particles in the DMTPC detector using a "Canary" detector that has a TPC built from the same materials. I measure the energy spectrum and rate of alpha background in DMTPC. It was found that the rate of alphas are coming primarily from the drift cage rings, because replacing stainless steel rings with copper reduced the rate by a factor 5. Copper is known to have lower concentrations of uranium and thorium than stainless steel and - as a consequence - lower α background.

The rate was found to be constant in time, disfavoring the idea that radon builds up in the vessel. Moreover, from energy distributions we know that if we were to have buildup of radon into the chamber, we'd have a lot more alphas around the the 7MeV range. This, however, is not the case, as can be seen in Figures 3-9 and 3-8.

Based on the work described in this thesis, we conclude that the bulk of alphas are coming from the decay of material (such as uranium and thorium in stainless steel) from inside of the chamber. Moreover, replacing radon-generating material such as stainless steel with copper within the detector greatly reduces the level of background and keeps it at a relatively constant rate. This is in contrast to previous experiments, such as NEWAGE [10] and DRIFT [9] that see alpha rates rising with time.

Appendix A

FINITE ELEMENTS METHOD

A.1 Electric Field Calculation

The Finite Element Method (FEM) is a mathematical technique for numerically solving partial differential equation (PDE) problems that are either extremely difficult or impossible to solve algebraically. In general, a mathematical (continuous) domain is discretized into a set of finite elements. The numerical solutions at the near-boundary points are found by extrapolating known solutions at the boundary. Once the near-boundary points have definitive solutions, we can then approximate the numerical solutions in the neighboring points those. Continuing this process we can finally find the solution at (or very near to) our desired point inside our geometry.

If, however, we wish to construct a full model that represents the behavior of our mathematical problem across a specific geometry, we can construct a mesh of such finite element points and find numerical solutions to all of them using large matrices. A brief outline of the steps is given below. A more comprehensive introductory guide to the Finite Element Method may be found at [12].

For the following derivation, I will be referring to the first three of Maxwell's equations.

Gauss' Law:

$$\nabla \cdot \mathbf{E} = \frac{\rho}{\varepsilon_0} \tag{A.1}$$

Gauss' Law for Magnetism:

$$\nabla \cdot \mathbf{B} = 0 \tag{A.2}$$

Faraday's Law of Induction:

$$\nabla \times \mathbf{E} = -\frac{\partial \mathbf{B}}{\partial t} \tag{A.3}$$

Equation (A.2) shows that the magnetic field vector, $\mathbf{B}$, is a solenoidal vector. This means that, using Helmholtz's theorem, $\mathbf{B}$ can be expressed in terms of the curl of a vector field:

$$\mathbf{B} = \nabla \times \mathbf{A}$$

Where $\mathbf{A}$ is called the Magnetic Potential. Next, we take the negative derivative of both sides in terms of time:

$$-\frac{\partial \mathbf{B}}{\partial t} = -\nabla \times \frac{\partial \mathbf{A}}{\partial t}$$

Taking advantage of Faraday's Law (A.3), we get:

$$\nabla \times \mathbf{E} = -\nabla \times \frac{\partial \mathbf{A}}{\partial t}$$

$$\nabla \times \left(\mathbf{E} + \frac{\partial \mathbf{A}}{\partial t} \right) = 0$$

Here again we can use Helmholtz's theorem to express the curl-free parenthetical unit as the gradient of a scalar function:

$$\mathbf{E} + \frac{\partial \mathbf{A}}{\partial t} = -\nabla \mathbf{\Phi}$$

Where Φ is called the Charge Potential. Taking the gradient of both sides, we get:

$$\nabla \mathbf{E} + \nabla \frac{\partial \mathbf{A}}{\partial t} = -\nabla^2 \mathbf{\Phi}$$

Now we can plug in Gauss' Law (A.1) to get:

$$\frac{\rho}{\varepsilon_0} + \frac{\partial}{\partial t}(\nabla \mathbf{A}) = -\nabla^2 \mathbf{\Phi}$$

$$\nabla^2 \mathbf{\Phi} + \frac{\partial}{\partial t}(\nabla \mathbf{A}) = -\frac{\rho}{\varepsilon_0}$$

Since we do not concern ourselves with the magnetic potential, $\mathbf{A} = 0$. We now have a much more simplified

$$\nabla^2 \mathbf{\Phi} = -\frac{\rho}{\varepsilon_0} \tag{A.4}$$

The relationship presented in (A.4) is, generally speaking, a PDE of the form:

$$u'' = f \tag{A.5}$$

Where u is our potential and f is our charge. Now, if we multiply both sides of the equation with a special function v_k (See Figure A-1; a more detailed discussion of this function will follow shortly), we'll get:

$$u'' v_k = f v_k$$

$$\int u(x) v_k(x)\,\mathrm{d}x = \int f(x) v_k(x)\,\mathrm{d}x$$

Performing integration by parts we get:

$$-\int u'(x) v_k'(x)\,\mathrm{d}x + u(x) v_k(x)\Big|_{initial}^{final} = \int f(x) v_k(x)\,\mathrm{d}x$$

Since v_k is a smooth function that is 0 at boundaries (see figure A-1, the second term on the left-hand side disappears, leaving:

$$-\int u'(x) v_k'(x)\,\mathrm{d}x = \int f(x) v_k(x)\,\mathrm{d}x \tag{A.6}$$

Let's step back and look at the special v_k function again. Suppose that we know the values of a function $u(x)$ at the points $k-1$, k, $k+1$, and so forth (figure A-1. Now

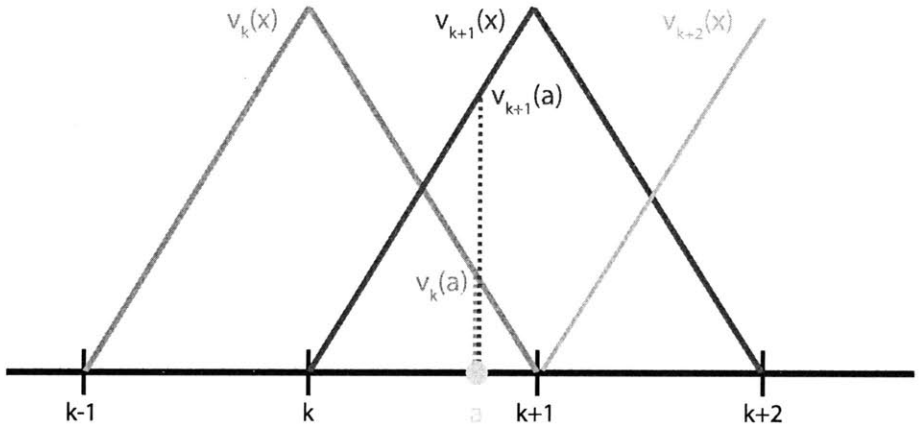

Figure A-1: An example of a smooth interpolation function v_k that satisfies boundary conditions of being 0 at its edges and 1 at its apex. Its main purpose is to help interpolate the value of a function at a point a, given values at neighboring points $k-1$, k, $k+1$, etc.

we wish to find the value of $u(x)$ at some arbitrary point a. In other words, we need to interpolate the value of the function $u(x)$ at point a given values at neighboring points k and $k+1$. So, all we need is some function $v(x)$ that will allow us to weigh the neighboring points appropriately[1] to find a good "fit" for the function value at point a. In other words:

$$u(a) = u(k) \cdot v_k(a) + u(k+1) \cdot v_{k+1}(a)$$

Or, in general, for any point x, given a set of known function values at points $k_i, k_{i+1}, \ldots, k_f$:

$$u(x) = \sum_{j=k_i}^{k_f} u_j v_j(x) \tag{A.7}$$

Similarly,

$$f(x) = \sum_{j=k_i}^{k_f} f_j v_j(x) \tag{A.8}$$

[1]The function presented in figure A-1 weighs neighboring points based merely on Euclidean distance of the immediate neighbors. Specifically it discounts values at $k-1$ and $k+2$ and takes a higher fraction of the value at $k+1$ into account since a is closer to $k+1$. One can certainly come up with more complex interpolation functions that work in the same basic way.

Additionally, one can take the derivative of both sides of equation (A.7) to get:

$$u'(x) = \sum_{j=k_i}^{k_f} u_j v_j'(x) \tag{A.9}$$

Returning now to equation (A.6), we can plug in equations (A.8) and (A.9) to get:

$$\int \sum u_j v_j'(x) v_k'(x)\,\mathrm{d}x = -\int \sum f_j v_j(x) v_k(x)$$

Taking the constant values out of the equation,

$$u \int \sum v_j'(x) v_k'(x)\,\mathrm{d}x = -f \int \sum v_j(x) v_k(x)$$

Where $u \equiv \sum u_j$ and $f \equiv \sum f_j$.

We can now replace $M_{jk} \equiv \int \sum v_j'(x) v_k'(x)\,\mathrm{d}x$ and $L_{jk} \equiv -\int \sum v_j(x) v_k(x)\,\mathrm{d}x$. Thus:

$$uM_{jk} = fL_{jk} \Rightarrow \begin{bmatrix} u = fLM^{-1} \\ f = uML^{-1} \end{bmatrix} \tag{A.10}$$

The two relations given in equation (A.10) can be plugged into a computer, and, given a geometry and boundary conditions, the computer will be able to interpolate the values of both charge (f) and potential (u) within the geometry.

In our case, the problem can be solved in three general steps:

1. Find the charge at the boundary where the voltage is known,
2. Knowing the charge, we can now find the voltage *near* the boundary.
   By repeating steps (1) and (2) we can
3. Build a mesh and find the voltage at any point inside the drift cage geometry

A.2 FreeFEM++

FreeFEM++ is a free software for modeling and numerically solving FEM problems. It is an Integrated Development Environment (IDE) architecture with its own high-

level language based on C++. The software is intended for scientific use and is quite intuitive. It serves well for the purposes of modeling the geometry of our drift region and solving for the electric field within it using the finite element method.

Besides being numerically robust, FreeFEM++ also has a good graphical package, the advantages of which will be shown in the next section.

Appendix B

HOUGH TRANSFORM

Search for alpha tracks is done by applying the Hough transform algorithm. The Hough transform can be used to search for any shape, and straight tracks are one of simplest applications. In this procedure, cartesian coordinates are transoformed into a different set of coordinates in which certain features of the images are enhanced. In the first step images are cleaned up by subtracting bias frame (Figure B-1a), and removing pixels that are consistent with readout noise (Figure B-1b)). Coordinates of remaining pixels are transformed into angles with respect to an arbitrary point (Figure B-1b)):

$$\theta = \arctan\left(\frac{\Delta y}{\Delta x}\right)$$

where Δx and Δy are distances of the pixel center from the origin. If all points lie on a line, their angles are the same and a problem of track-finding in a 2-dimensional plane is transformed to a peak finding in a 1-dimensional histogram. Figure B-1c) shows a histogram of transform angles. The finite width of the peak is due to detector resoution and straggling of alpha track.

After candidate pixels are identified, track pixels are fitted with a straight line to improve precision of track parameters. Energy of the track is computed from track residuals from the fitted line, using the original image. The residuals are modeled with a Gaussian function for signal, and a constant function for readout noise. Pixels above threshold with maximum separation are taken as endpoints, and therefore the

range of the track.

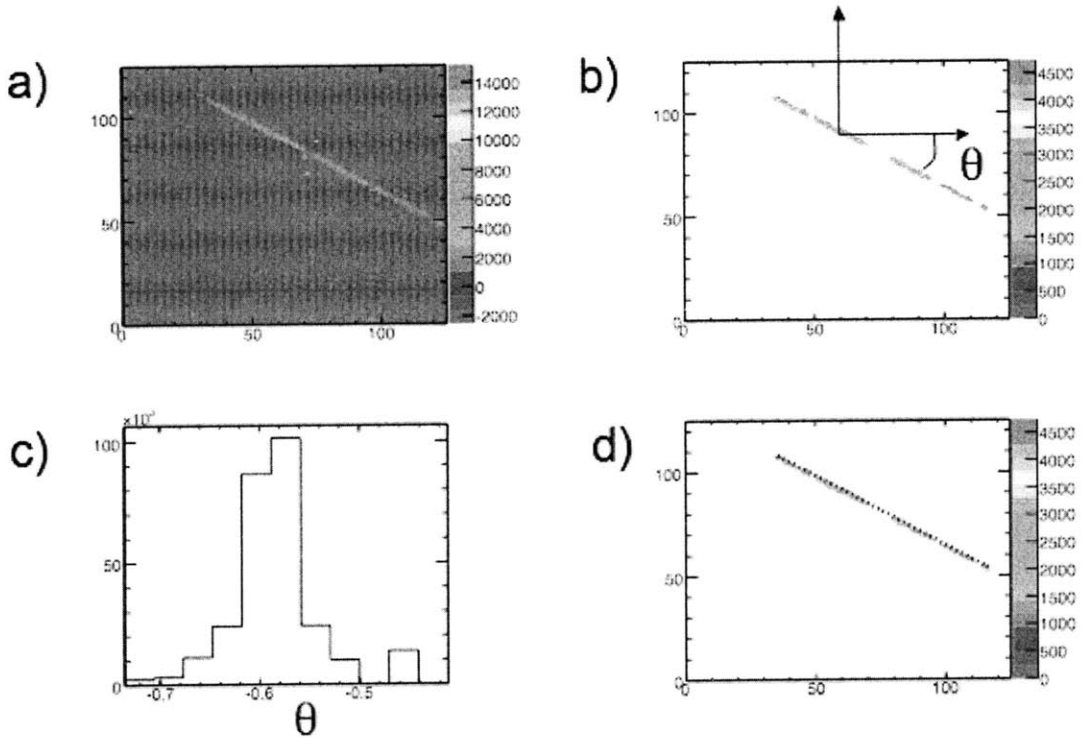

Figure B-1: Steps in track search algorithm: (a) raw image after bias frame subtraction, (b) image after removal of under-the-threshold pixels, (c) histogram of angles for remaining pixels, (d) fitted track.

Appendix C

DARK MATTER EXPERIMENTS

There are a multitude of experiments throughout the world that are trying to detect WIMPs. All of these can be classified under two groupings: direct detection, and indirect detection methods. Indirect detection experiments rely on the fact that dark matter particles are Majorana fermions and can thus annihilate themselves. These annihilations create products such as gamma rays, proton-antiproton, and electron-positron pairs. The antiparticle formation, as well as the gamma ray release within the center of the universe - where dark matter is concentrated - or anywhere else in the halo, could be indicative of WIMP presence.

The two biggest experiments in this field are the GLAST (Gamma-ray Large Area Space Telescope) and PAMELA (Payload for Antimatter Matter Exploration and Light-nuclei Astrophysics) group. GLAST looks for a continuous stream of gamma rays of specific wavelengths produced in predicted clumps of dark matter in and around galaxies. PAMELA, on the other hand, is looking for the antiparticle products such as anti-protons and positrons. Two years of data released from the satellite show a promising excess of positrons, but no such excess of anti-protons. The lack of anti-protons, as well as the complexity of identifying the source of most positrons renders the results of the PAMELA group inconclusive.

The other classification of experiments is the direct detection. This classification

contains several families of experiments. There are the cryogenic experiments such as CDMS (Cryogenic Dark Matter Search) underneath Stanford University campus, EDELWEISS (Exprience pour DEtecter Les Wimps En Site Souterrain) in Modane Underground Laboratory, EURECA (European Underground Rare Event Calorimeter Array) also in Modane, and CRESST (Cryogenic Rare Event Search with Superconducting Thermometers) in the undergrounds of Gran Sasso National Laboratory. The cryogenic detectors look for signature WIMP interactions with the molecules of a target crystal that would heat it up by a very specific temperature. These events should be extremely rare happening once per day per 10 kilograms of target material. The cryogenic experiments are all housed underground to reduce background caused by cosmic rays.

The second family of experiments in the direct detection class is the scintillation detectors like XENON in Gran Sasso, ArDM (Argon Dark Matter), and LUX (Large Underground Xenon Detector). This family of experiments uses large detectors filled with a noble gas such as xenon or argon to detect a WIMP particle passing through. In the event of a collision between a passing particle and one of the molecules of the detector gas, light scintillates and is detected by an array of photomultiplier tubes (PMTs). The detector can accurately discriminate between nuclear (WIMPs and neutrons) and electron (gamma and beta background), however, it has trouble telling apart WIMPs from neutrons or some other nuclear recoil.

A subgroup in the family of scintillation detectors is a handful of experiments that look not only for these recoil events, but also for the direction from where the intruding particle came from. Two of the prominent experiments in this field are DRIFT (Directional Recoil Identification From Tracks) at Boulby Underground Laboratory and DMTPC (Dark Matter Time Projection Chamber), to be commissioned at SUSEL (Sanford Underground Science and Engineering Laboratory) in South Dakota.

Bibliography

[1] F. Zwicky, Helv. Phys. Acta **6**, 110 (1933).

[2] V. C. Rubin and W. K. J. Ford, Astrophys. J. **159**, 379 (1970).

[3] A. Refregier, Ann. Rev. Astron. Astrophys. **41**, 645 (2003) [arXiv:astro-ph/0307212].

[4] J. A. Tyson, G. P. Kochanski and I. P. Dell'Antonio, Astrophys. J. **498**, L107 (1998) [arXiv:astro-ph/9801193].

[5] D. Clowe, M. Bradac, A. H. Gonzalez, M. Markevitch, S. W. Randall, C. Jones and D. Zaritsky, Astrophys. J. **648**, L109 (2006) [arXiv:astro-ph/0608407].

[6] E. Komatsu *et al.*, arXiv:1001.4538 [astro-ph.CO].

[7] R. J. Gaitskell, Ann. Rev. Nucl. Part. Sci. **54**, 315 (2004).

[8] D. N. Spergel, Phys. Rev. D **37**, 1353 (1988);

[9] S. Burgos *et al.*, Astropart. Phys **28** 409-421 (2007);

[10] K. Miuchi *et al.*, Phys. Lett. B **686**, 11 (2010) [arXiv:1002.1794 [astro-ph.CO]].

[11] D. Dujmic *et al.*, Astropart. Phys. **30**, 58 (2008) [arXiv:0804.4827 [astro-ph]].

[12] G. P. Nikishkov Introduction to the Finite Element Method (2009)